Applied Catalysis B: Environmental 244 (2019) 107–119

Contents lists available at ScienceDirect

Applied Catalysis B: Environmental

journal homepage: www.elsevier.com/locate/apcatb

Simulation and optimization of the post plasma-catalytic system for toluene degradation by a hybrid ANN and NSGA-II method

Tian Chang[a,c], Jiaqi Lu[a], Zhenxing Shen[a,b,*], Yu Huang[b], Di Lu[a], Xin Wang[d], Junji Cao[b], Rino Morent[c]

[a] Department of Environmental Sciences and Engineering, Xi'an Jiaotong University, Xi'an, 710049, China
[b] Key Lab of Aerosol Chemistry & Physics, Institute of Earth Environment, Chinese Academy of Sciences, Xi'an, 710049, China
[c] Research Unit Plasma Technology, Department of Applied Physics, Faculty of Engineering and Architecture, Ghent University, Sint-Pietersnieuwstraat 41 – B4, 9000 Ghent, Belgium
[d] Multiphase Chemistry Department, Max Planck Institute for Chemistry, Mainz, 55128, Germany

ARTICLE INFO

Keywords:
Post-plasma-catalytic system
Dielectric barrier discharge
Toluene removal
Artificial neural network
Non-dominating sorting genetic algorithm II

ABSTRACT

In this study, a post-non-thermal plasma (NTP)-catalytic system was developed for the removal of toluene over a series of $MnCoO_x/\gamma\text{-}Al_2O_3$ catalysts. The addition of the $MnCoO_x/\gamma\text{-}Al_2O_3$ catalysts markedly promoted the toluene removal efficiency, CO_x yield, CO_2 yield and energy yield (EY) compared with the plasma alone system. The 5 wt% $MnCoO_x/\gamma\text{-}Al_2O_3$ catalyst exhibited the best reaction performance, which could be attributed to the reducibility and surface active oxygen species of the catalyst. With artificial neural network (ANN), the effects of experimental parameters on the reaction performance of toluene degradation were modeled and analyzed; for this analysis, four parameters were considered, namely, discharge power, initial concentration of toluene, flow rate, and relative humidity. The results indicated that the predicted results fitted well with the experimental results. The discharge power was the most significant factor for the toluene removal efficiency and CO_x yield, whereas the EY was the most influenced by the gas flow rate. A multi-objective optimization model was proposed to determine optimal experimental parameters, which was then solved using the non-dominating sorting genetic algorithm II (NSGA-II). The results revealed that the Pareto front obtained from the hybrid ANN and NSGA-II method provided a series of feasible and optimal process parameters for the post-NTP-catalytic system. This hybrid method also served as an effective tool to select process parameters according to application conditions and preferences.

1. Introduction

Volatile organic compounds (VOCs), as common air pollutants, can negatively impact both the human health and ecological environment [1–4]. Many environmental problems such as the formation of organic aerosols, photochemical smog and tropospheric ozone are caused by VOCs because of their toxicity [5–9]. Consequently, great efforts have been devoted to the development of methods for its removal. However, traditional technologies such as absorption, adsorption, condensation, photocatalytic oxidation, and catalytic combustion are inadaptable and uneconomical for treating dilute VOCs in high volume gas streams [10,11]. Non-thermal plasma (NTP) technology, as a promising alternative technology, has been applied for VOCs degradation in recent years owing to its unique advantages such as quick start-up, low reaction temperature and a wide range of application [12–15]. However, the formation of undesirable by-products is a disadvantage in the plasma process [16,17].

To overcome the above problem, an NTP-catalyst technology has been developed. The combination of NTP and catalyst includes two different configurations: introducing the catalyst inside the discharge region (IPC) or downstream the discharge region (PPC) [18–21]. For the former, the catalyst can influence the NTP properties, and meanwhile, the NTP can influence the catalyst properties [22]. The active species generated in the discharge region can be adsorbed on the catalyst surface, which can prolong the reaction time between pollutants and active species. For the latter, the NTP and catalyst are relatively independent compared with the IPC configuration. Only long-lived species (such as O_3) generated in the discharge region can reach the catalyst surface, which can be dissociated into active oxygen species by catalyst to favor the further oxidation of pollutants. Both the IPC and

* Corresponding author at: Department of Environmental Sciences and Engineering, Xi'an Jiaotong University, Xi'an, 710049, China.
E-mail address: zxshen@mail.xjtu.edu.cn (Z. Shen).

https://doi.org/10.1016/j.apcatb.2018.11.025
Received 9 July 2018; Received in revised form 5 November 2018; Accepted 9 November 2018
Available online 14 November 2018

PPC configurations can lead to the synergistic effect of NTP and catalyst including improving the pollutants removal efficiency and mineralization degree. Moreover, compared with IPC configuration, PPC configuration has received increasing attention because of the three reasons as follows: easier operation, preferable to practical application, and more effective control of byproducts [14,23]. The catalyst performs a key role in the NTP-catalyst system especially in the post-NTP-catalyst system, because it has enormous potential cooperating with NTP to enhance the synergistic effect [24]. Manganese oxide-based materials showed advantages over other transition metal oxide catalysts, including higher cooperative reaction performance, low cost, and greater environmental benefits [25–30]. Recent work [31,32] has shown that the introduction of Co species into Mn species could remarkably enhance the catalyst activity in comparison to pure Mn species. The metal oxide loaded on the support materials usually exhibit higher performance than the metal oxide alone [33–35]. In addition, γ-Al_2O_3 stands out for its high activity and chemical stability in VOCs removal [36]. However, little work has been done to apply the $MnCoO_x/\gamma$-Al_2O_3 system to toluene degradation.

The physico-chemical reactions in the NTP-catalyst system are complicated and controlled by various process parameters. Most conventional work has concentrated on the effect of individual experimental parameters on the NTP-catalyst performance, and little on the interactions of various parameters [6,37]. Thus, it is essential to develop a comprehensive model to predict the response results and optimize the operation parameters in the NTP-catalytic system. Artificial neural networks (ANNs) are regarded as a potential tool in the process simulation and prediction based on their self-adaptive, self-organizing, and self-learning ability [38]. ANNs were chosen to implicitly detect all possible interactions between input process parameters and output performance [39]. A recent study [1] demonstrated that an ANN model could effectively simulate the influences of different process parameters (discharge power, flow rate, initial concentration, Mn percentage) on a methanol removal process in a post-plasma-catalytic system. Both removal efficiency, CO/CO_2 yield and energy yield (EY) are objectives of toluene removal; therefore, a multi-objective model should be adopted to optimize the process parameters. The non-dominating sorting genetic algorithm II (NSGA-II) algorithm is considered a widely used and effective algorithm to solve multi-objective programming. Therefore, a method using ANNs coupled with the NSGA-II algorithm is expected to be a promising and powerful technique for complex process modeling and optimization. However, it has received little attention for the prediction and optimization of the chemical reactions in the NTP system, especially for the NTP-catalytic system.

In this study, toluene was chosen as a representative of VOCs because of its high toxicity to human health. A post-NTP-catalytic system with different catalysts was built to investigate the influence of different operating parameters in terms of the toluene removal efficiency, EY, as well as CO and CO_2 yields (CO_x yield). First, a series of $MnCoO_x/\gamma$-Al_2O_3 catalysts were prepared using the deposition–precipitation method and characterized to further understand its catalytic activities. Then, ANN was used to model the effects of experimental parameters on the performance of toluene removal in the post-NTP-catalytic system, in which four parameters (discharge power, initial concentration, gas flow rate and relative humidity (RH)) were considered. Based on the ANN model, a multi-objective programming model was proposed to determine the optimal process parameters, and the NSGA-II algorithm was developed to solve the multi-objective problem. Thus, the optimal operating parameters in the NTP-catalytic system were obtained through the hybrid ANN and NSGA-II methods.

2. Experimental

2.1. Experimental set-up

The schematic diagram of the experiment was presented in Fig. 1. The details of the dielectric barrier discharge (DBD) reactor (Nanjing Suman Electronic Co., China) have been described in our previous work [40]. A 150 mm long stainless-steel mesh was wrapped around a quartz tube (inner diameter of 30 mm and outer diameter of 35 mm) as a high-voltage electrode. A stainless-steel wire with an outer diameter of 1 mm was coiled around the inner surface of the quartz tube (inner diameter of 10 mm and outer diameter of 14 mm) as a ground electrode. The DBD discharge gap was 8 mm and filled with glass beads (diameter of 5 mm). The DBD reactor was connected to an AC high voltage power supply with a frequency of 10 kHz (CTP-2000 K, Nanjing Suman Electronic Co., China). All the electrical signals were recorded on an oscilloscope (Tektronix MDO3012). The discharge power of the DBD reactor was calculated using the classical V-Q Lissajous method based on the Eq. (1) [41].

$$P = f \times C \times A \tag{1}$$

where f was 10 kHz, C was 0.47 u F and A donated area of the Lissajous diagram. The voltage-charge Lissajous figure was shown in Fig. A1.

The post-NTP-catalytic system was operated at room temperature and atmospheric pressure. The carrier gas was dry air (N_2: O_2 = 4:1). The carrier air and toluene were uniformly mixed prior to introducing them in the DBD reactor. The initial concentration of toluene was obtained by regulating the flow rate of the carrier air and toluene controlled by a mass flow controller (MFC, Sevenstar D07-series). RH was controlled by tuning the ratio of gas flow rate of dry air and air passing through a water bath; the RH was monitored using a Q-track (Model 7565, TSI Inc., USA). The catalysts (100 mg, 40–60 mesh) were placed in the rear of the discharge region and held in place with quartz wool. The distance between the catalyst and discharge area was approximately 5 mm. The toluene concentration at the inlet and outlet of the experimental system was measured online with gas chromatography (GC, FULI-9790). An online Fourier transform infrared spectrometer (FTIR, PerkinElmer Spectrum Two, USA) was used to measure the CO/CO_2 concentration. Before sampling, the FTIR was calibrated with standard CO/CO_2 gas. The organic byproducts from the outlet were absorbed by hexane and then qualitatively analyzed through a gas chromatography/mass spectrometry detection (GC–MS, Agilent 6890 A GC/5973 MS). This instrument was equipped with an HP-5 MS capillary column (50 m × 0.32-mm inner diameter, 0.25-μm film thickness). The ion source temperature was 250 °C and the electron impact mode was 70 eV. The injector temperature and detector temperature were set to 100 °C and 240 °C, respectively. The initial temperature of the GC oven was held at 40 °C for 4 min, and then the temperature increased to 220 °C with a rate of 10 °C·min^{-1} and hold for 5 min. MS identification was conducted using the NIST 14 databank.

All the experimental data were acquired by calculating the average value of three repeated measurements. In this study, the toluene removal efficiency ($\eta_{toluene}$), specific energy density (SED), EY and CO_x yield were calculated as follows:

$$\eta_{toluene}(\%) = \frac{[\text{toluene}]_{inlet} - [\text{toluene}]_{outlet}}{[\text{toluene}]_{inlet}} \times 100\% \tag{2}$$

$$\text{SED}(\text{J}\cdot\text{L}^{-1}) = \frac{\text{discharge power(W)}}{\text{gas flow rate}(\text{L}\cdot\text{min}^{-1})} \times 60(\text{s}\cdot\text{min}^{-1}) \tag{3}$$

$$\text{EY}(\text{g}\cdot\text{kWh}^{-1}) = \frac{M_{toluene} \times \eta_{toluene}}{\text{SED}} \times \frac{3.6}{V_m} \tag{4}$$

$$\text{CO yield}(\%) = \frac{[\text{CO}]}{7([\text{toluene}_{inlet}] - [\text{toluene}_{outlet}])} \times 100\% \tag{5}$$

$$CO_2\text{yield}(\%) = \frac{[CO_2]}{7([\text{toluene}]_{inlet} - [\text{toluene}_{outlet}])} \times 100\% \tag{6}$$

$$CO_x\text{yield}(\%) = \frac{[\text{CO}] + [CO_2]}{7([\text{toluene}_{inlet}] - [\text{toluene}_{outlet}])} \times 100\% \tag{7}$$

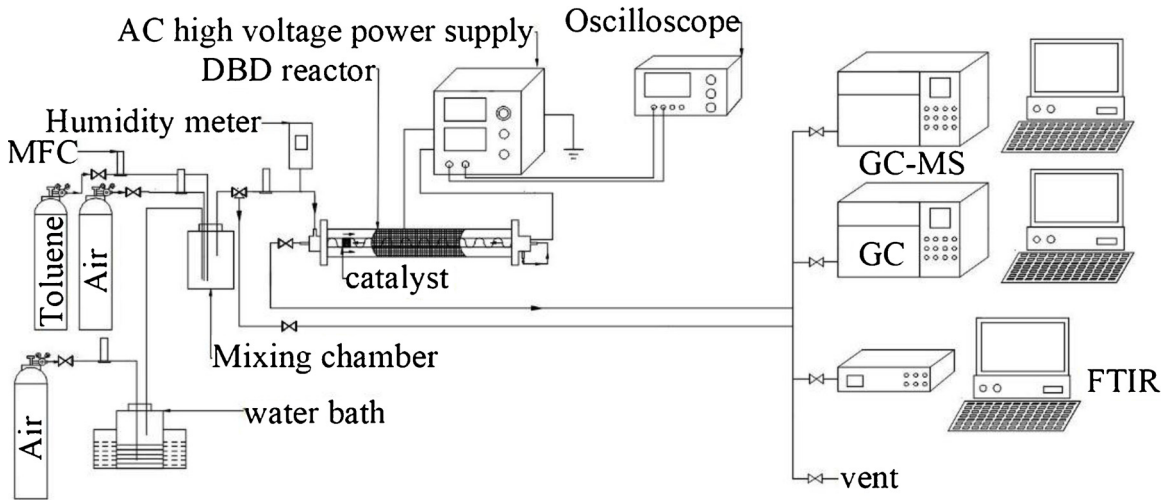

Fig. 1. Schematic diagram of the experiment.

where V_m donated as the molar volume ($L{\cdot}mol^{-1}$).

2.2. Catalyst preparation and characterization

The $MnCoO_x/\gamma\text{-}Al_2O_3$ catalysts were prepared using the deposition–precipitation method. Different mass ratios of (Mn + Co) atoms were loaded on the $\gamma\text{-}Al_2O_3$ support with a fixed molar ratio of Mn/Co = 1 in all the prepared catalysts. The aqueous solutions of $Mn(NO_3)_2$ ($0.6\ mol{\cdot}L^{-1}$), $Co(NO_3)_2$ ($0.5\ mol{\cdot}L^{-1}$), and $KMnO_4$ ($0.4\ mol{\cdot}L^{-1}$) were used as the precursors. A typical synthesis involved the following steps. The mixed precursors were gradually added onto the support with stirring at 60 ℃ for 2 h. Subsequently, an aqueous solution of Na_2CO_3 ($1\ mol{\cdot}L^{-1}$) was added to the above turbid liquid dropwise. Then, the obtained turbid liquid was aged for 4 h under stirring. This mixture was then filtered, dried at 70 ℃ overnight, and calcined at 500 ℃ for 3 h. The obtained catalysts were crushed and sieved in 40–60 meshes for testing. All the achieved catalyst was denoted as x (2.5, 5, and 7.5) wt% $MnCoO_x/\gamma\text{-}Al_2O_3$, where x represented the mass ratio of (Mn + Co) atoms.

The crystal textures of all the catalysts were determined using X-ray powder diffraction (XRD; PAN analytical, X'pert, Almelo, the Netherlands). This instrument was equipped with a *Cu-Kα* radiation source (λ = 1.5406 Å) at an accelerating voltage and a current of 40 kV and 40 mA, respectively. Raman spectra were measured on a Laser Raman Spectrometer (HR Evolution, HORIBA, France) with an excitation of 514 nm laser light. The MnO_2–Co_3O_4 loading was measured using inductively coupled plasma emission spectrometry (ICP, Shimadzu E 9000, Japan). The specific surface area, total pore volume and average pore diameter of all the catalysts were acquired from N_2 adsorption–desorption isotherms at 77 K using an SSA-4200 analyzer (Beijing Builder, China). The morphology of all the catalysts was observed through field-emission scanning electron microscopy (SEM, Gemini SEM 500, German). Hydrogen temperature-programmed reduction (H_2-TPR) studies were conducted on the Micromeritics AutoChem 2910 instrument equipped with a thermal conductivity detector (TCD). X-ray photoelectron spectroscopy (XPS) was performed on AXIS ULtrabld XPS (ESCALAB Xi+, Thermo Fisher Scientific, America) equipment to obtain the elements' composition and chemical valence states on the catalyst surface. The C1s photoelectron peak at 284.8 eV was used as the reference of all binding energies.

2.3. Hybrid ANN and NSGA-II method

In this study, the effect of four experimental parameters, namely, discharge power, initial concentration, flow rate, and RH, on the reaction performance and their relative importance were evaluated using the hybrid ANN and NSGA-II methods by following the following steps: 1) an ANN model was employed to simulate the reaction in the post-NTP-catalytic system; and 2) the optimal process parameters were acquired by optimizing the input space within the ANN model using the NSGA-II algorithm.

A three-layer ANN model was developed for simulating the effects of experimental parameters on the reaction performance of toluene degradation. As shown in Fig. 2, the ANN model includes three layers: input, hidden and output layers. The input layer receives process parameters (discharge power, initial concentration of toluene, flow rate and RH) and the output layer gives response variables (toluene removal efficiency, EY, and CO_x yield). However, the hidden layer was behind no obvious physical meaning. The model was developed using the MATLAB neural network toolbox to model the reaction in the post-NTP-catalytic system. The feedforward ANN model was trained with a back-propagation training function using MATLAB neural network toolbox.

For training the ANN, 120 sets of experimental data were used. To ensure the generalization and obtain the optimal size of the hidden layer, the following treatments were developed:

(a) Partition the available example input-output data into three sets, namely training, validation and test sets;
(b) Assign 3 to the size of the hidden layer k;
(c) Initialize a 4-k-2 layer ANN model with two random weight sets, $W_1 \in R^{4\times k}$ and $W_2 \in R^{k\times 2}$;
(d) Train the network iteratively with the training set until the mean square error (MSE) with respect to the validation set is smaller than a given precision or till the number of the epoch exceeds 100;
(e) Test the performance of the trained ANN model using the MSE with respect to the test set;
(f) Repeat (c)–(e) 10 times and record the best performance.
(g) Increment k and repeat (c)–(f) until k exceeds 20;
(h) Choose the ANN model with the best performance and record the corresponding k and weight matrices W_1 and W_2.

The NSGA-II algorithm is widely used in optimizing problems on the basis of the principle of survival of the fittest during evolution. In this study, toluene removal efficiency and EY were taken as objective functions. Because the toluene removal efficiency and the CO_x yield share the same trend as the EY yield varies, the CO_x yield was not considered as an independent objective. Decision variables comprise the four process parameters, namely, discharge power, initial concentration of toluene, flow rate, and RH.

In this study, the computer codes of genetic algorithm optimization

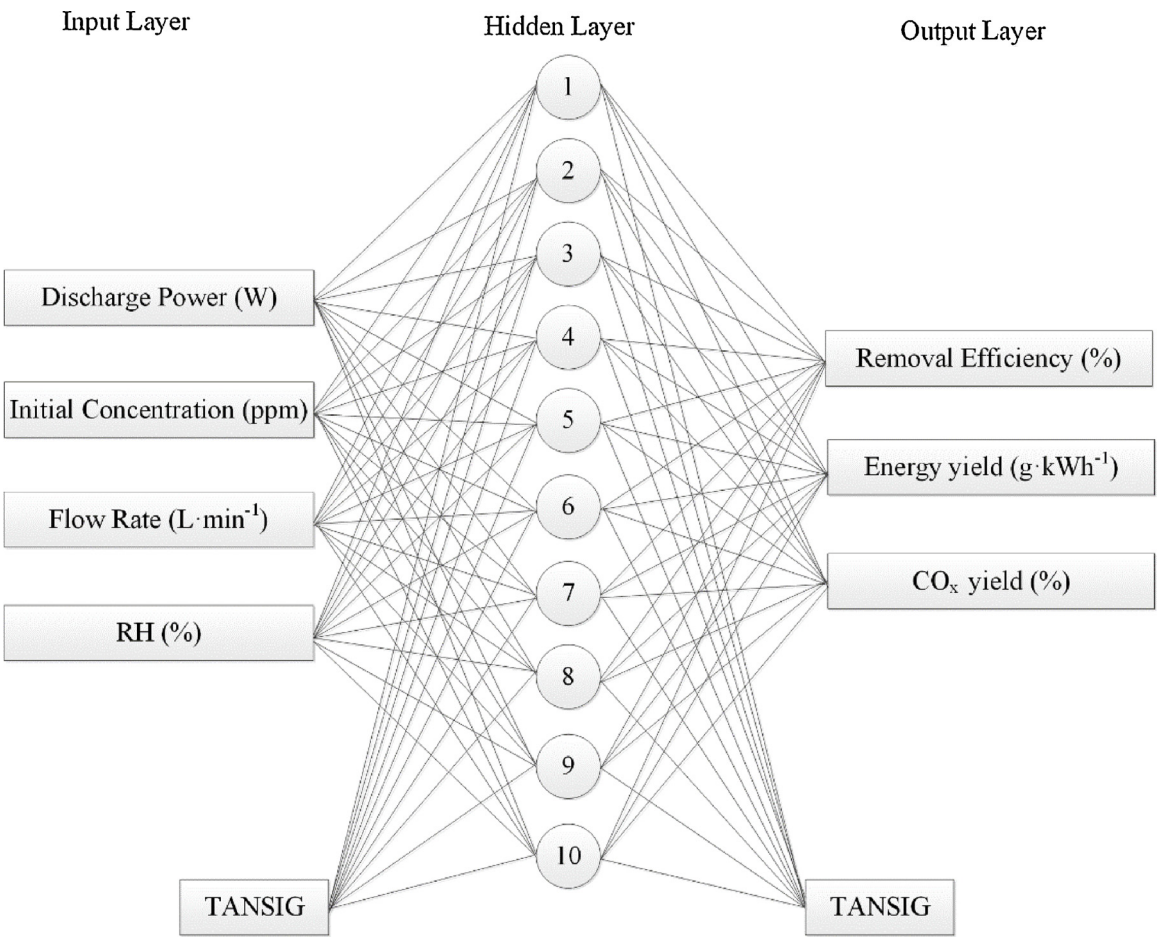

Fig. 2. Optimized three-layer ANN model with a tangent sigmoid transfer function (TANSIG).

were developed using MATLAB. The trained ANN model was embedded into the NSGA-II algorithm by serving as the objective function. The main steps of the NSGA-II are listed as follows.

(a) Randomly generate *N* (a given integer) individuals in the first generation. Here an individual is a tuple of numbers denoting the values of process parameters. We call all the individuals in a generation a population, denoted as set *P*;
(b) Obtain the objectives for each individual by calculating the output of the trained ANN model;
(c) Sort the population *P* into Pareto fronts with the fast non-dominated sorting algorithm, and then calculate the crowding distance of every individual in each Pareto fronts;
(d) Generate offsprings from generation *P* by selection, mutation, and crossover, and denote them with a set *Q*;
(e) Obtain the objectives for each individual in *P*∪*Q* by calculating the output of the trained ANN model;
(f) Sort *P*∪*Q* into Pareto fronts with the fast non-dominated sorting algorithm, and then calculate the crowding distance of every individual in each Pareto front;
(g) Select the *N* individuals from *P*∪*Q* by selecting dominating Pareto fronts first and selecting individuals with larger crowding distance. The new generation *P* comprises the *N* selected individuals;
(h) Repeat steps (d)–(g) until the number of generations reach the given times. Each individual in the first Pareto front of generation *P* is an optimal solution.

3. Results and discussions

3.1. Toluene decomposition over different catalysts

Fig. 3 showed the toluene removal efficiency, EY, and CO_x yield of different $MnCoO_x$ loading catalysts via the post-NTP-catalytic system. It was apparent that compared with those in the NTP alone system, the toluene decomposition, EY, and CO_x yield increased after the catalysts addition. The $MnCoO_x$ loading affected the catalytic activity significantly in the post-NTP-catalytic system. With the increase in the $MnCoO_x$ loading, the toluene removal efficiency, EY, CO_x yield and CO_2 yield first increased and then decreased, with 5 wt% $MnCoO_x/\gamma$-Al_2O_3 affording the best performance. In the NTP-5 wt% $MnCoO_x/\gamma$-Al_2O_3 system, the toluene decomposition, CO_x yield, CO_2 yield and EY increased by 25.74%, 14.77%, 16.30%, 0.45 g·kWh^{-1}, respectively, compared with those in the NTP alone system. This could be attributed to the fact that toluene and intermediates were further oxidized to CO_2 and H_2O via active species on the surface of the catalysts [42]. The different catalytic activity might be ascribed to the different physicochemical properties of the catalysts [2].

3.2. Catalysts characterizations

3.2.1. Crystal structure, tunnel structure and morphology of the as-prepared catalysts

The crystalline phases of the γ-Al_2O_3 and $MnCoO_x/\gamma$-Al_2O_3 catalysts were depicted in Fig. 4(a). All catalysts exhibited highly intense XRD diffraction peaks of γ-Al_2O_3 (JCPDS 00-010-0425) with typical cubic structure. No apparent characteristic diffraction peaks of manganese oxide or cobalt oxide existed at the low $MnCoO_x$ loading (2.5 wt%),

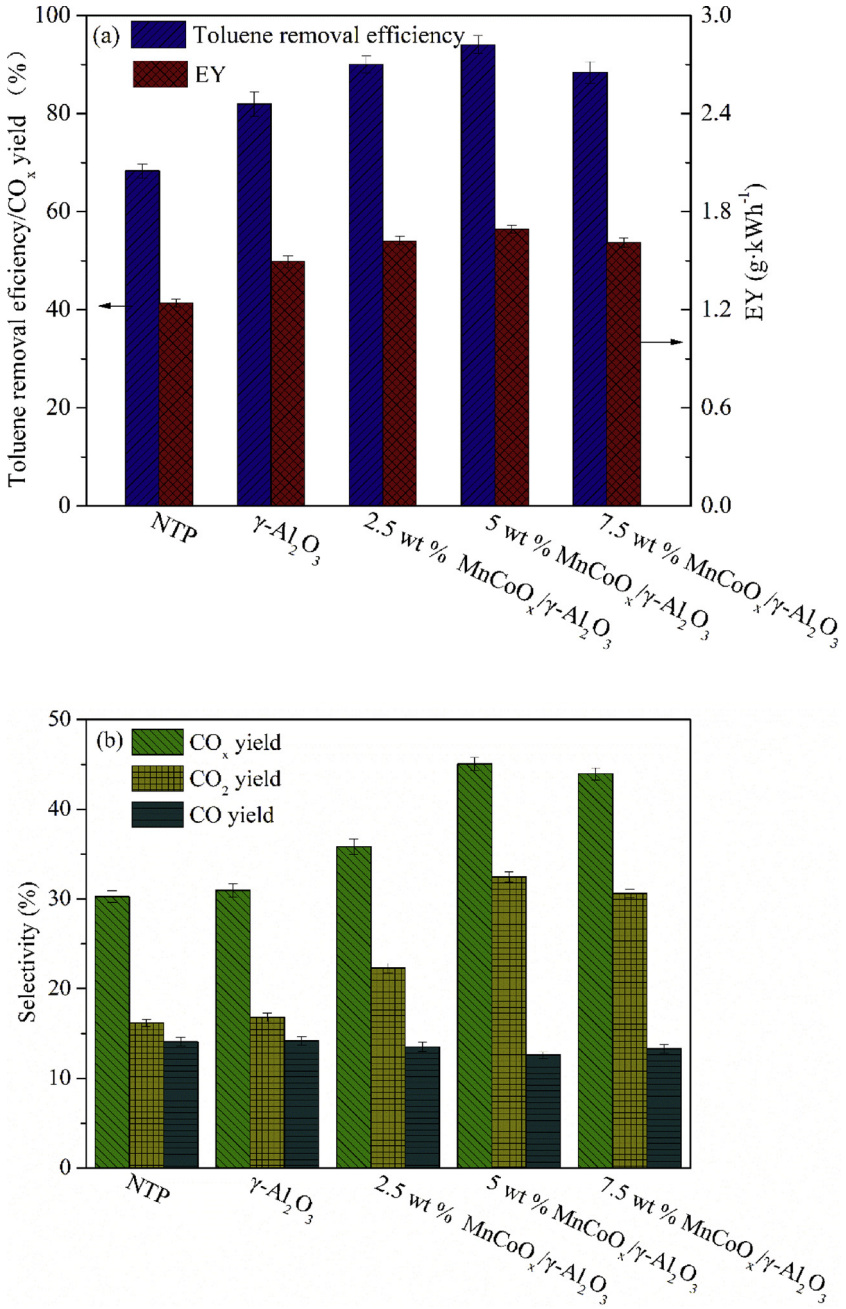

Fig. 3. Effect of catalysts on the toluene removal efficiency and EY (a), CO_x yield, CO yield and CO_2 yield (b) (discharge power, 10 W; toluene initial concentration, 54 ppm; gas flow rate, 1.5 L·min^{-1}; RH, 0%).

indicating the presence of manganese oxide and cobalt oxide with high dispersion. With the addition of $MnCoO_x$ loading, the diffraction peaks of Co_3O_4 (JCPDS 42-1467) were increasingly obvious, indicating the formation of bulk Co_3O_4. However, the diffraction peaks of MnO_2 (JCPDS 44-141) were still weaker, which could be attributed to the dispersion of Mn species into the Co_3O_4 lattice or the amorphous structure of MnO_2. This was in accordance with a previous report [43]. Notably, the typical diffraction peaks of (Co, Mn)(Co, Mn)$_2O_4$ (JCPDS 18-408) were clearly observed since the loading amount of Mn and Co atoms was more than 5%; this was probably because Mn cations moved into the Co_3O_4 lattice to form (Co, Mn)(Co, Mn)$_2O_4$. This would be conducive to defect generation and exposure [44], which could be beneficial to enhance the mineralization of toluene. In addition, the diffraction peaks of γ-Al_2O_3 became weaker and wider, indicating that the loading $MnCoO_x$ possessed poor crystallinity, and they dispersed on the surface of γ-Al_2O_3 to afford more active sites for the catalytic activity [45].

Raman spectroscopy was conducted to examine the phase composition of the catalysts. As shown in Fig. 4 (b), no peaks were observed in the γ-Al_2O_3 catalyst, whilst the three $MnCoO_x$/γ-Al_2O_3 catalysts showed similar profiles with three main peaks. The major Raman bands at 654 cm^{-1} were assigned to the Mn—O stretching vibration [46]. The Raman band located at 484 were consistent with one reported for Co_3O_4 [47]. In addition, based on the Raman spectra of Co_3O_4 and MnO_2, the Raman bands between 550–750 cm^{-1} of $MnCoO_x$/γ-Al_2O_3 included both the typical band of Co_3O_4 at 674 cm^{-1} and the typical band of MnO_2 at 645 cm^{-1}, indicating the existence of Co_3O_4 and MnO_2 on the γ-Al_2O_3 supports. In addition, the peaks of $MnCoO_x$/γ-Al_2O_3 were broader and weaker compared with the relevant peaks of the pure oxides, which could attribute to the interaction of Mn and Co species.

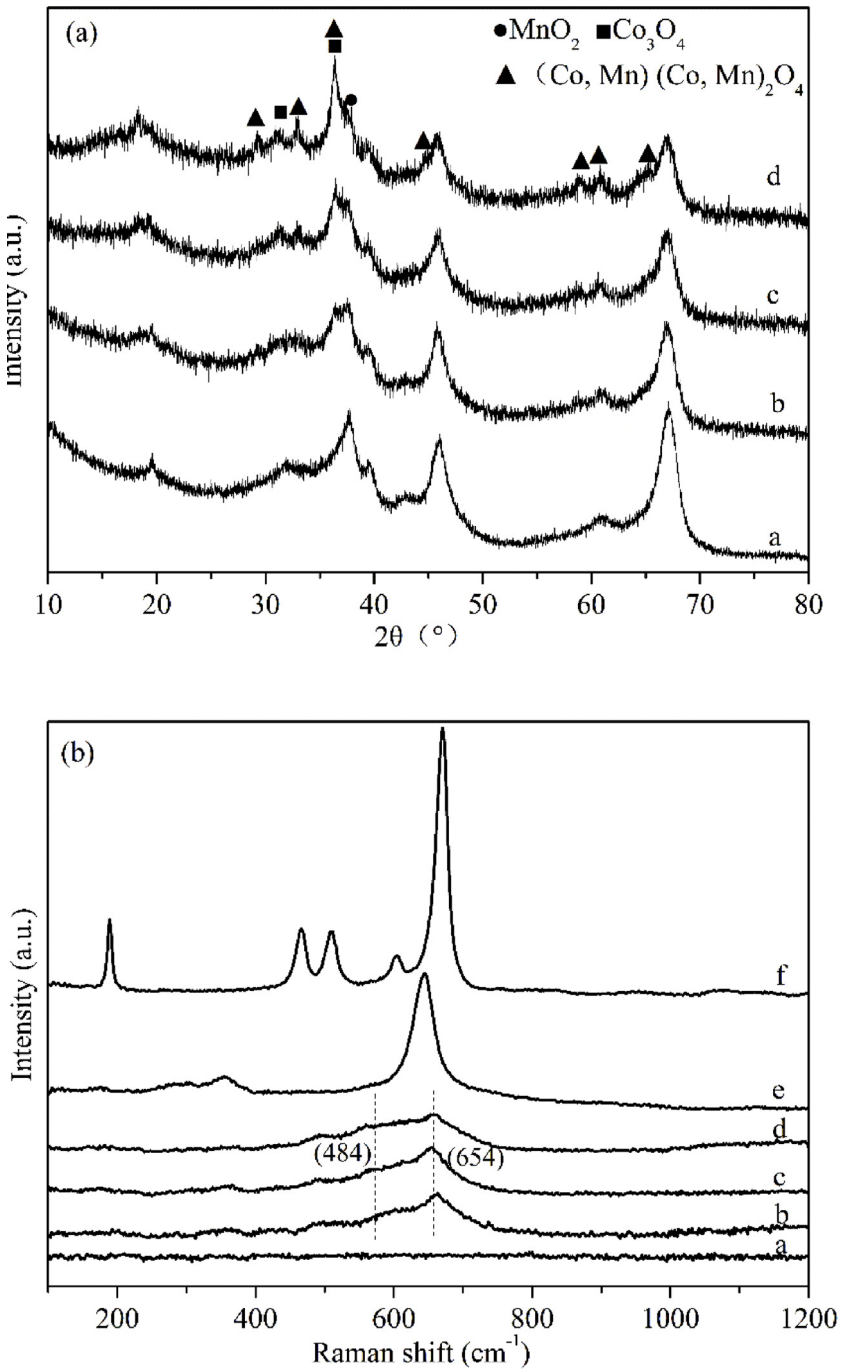

Fig. 4. XRD (a) and Raman (b) patterns of γ-Al_2O_3 and $MnCoO_x$/γ-Al_2O_3 catalysts (a: γ-Al_2O_3, b: 2.5 wt% $MnCoO_x$/γ-Al_2O_3, c: 5 wt% $MnCoO_x$/γ-Al_2O_3, d: 7.5 wt% $MnCoO_x$/γ-Al_2O_3, e: MnO_2, f: Co_3O_4).

Table 1
Physicochemical properties of γ-Al_2O_3 and $MnCoO_x$/γ-Al_2O_3 catalysts.

Sample	Mn and Co atom loading (ICP)	BET ($m^2 \cdot g^{-1}$)	Total pore volume ($cm^3 \cdot g^{-1}$)	Average pore diameter (nm)	[a]Particle size (nm)
γ-Al_2O_3	–	202.39	0.45	8.86	9.45
2.5 wt% $MnCoO_x$/γ-Al_2O_3	2.23	189.73	0.43	9.84	9.63
5 wt% $MnCoO_x$/γ-Al_2O_3	4.77	184.66	0.42	10.24	10.28
7.5 wt% $MnCoO_x$/γ-Al_2O_3	7.42	179.78	0.40	11.76	12.16

[a] Data calculated based on the XRD results according to the Scherrer equation using the FWHM of the average peak strength of sample.

As shown in Table 1, the $MnCoO_x$ loading was calculated using ICP analysis. The $MnCoO_x$ loading obtained from ICP was not exactly similar to the theoretical ration, but the deviation was acceptable. The γ-Al_2O_3 occupied a larger surface area (202.39 $m^2 \cdot g^{-1}$) compared with the $MnCoO_x$/γ-Al_2O_3. The surface area gradually decreased from 202.39 $m^2 \cdot g^{-1}$ to 179.78 $m^2 \cdot g^{-1}$ with the increasing $MnCoO_x$ loading, which could be ascribed to the fact that the $MnCoO_x$ overlapped the partial surface of the γ-Al_2O_3. Conversely, the average pore diameter increased from 8.86 to 11.76 nm, implying that the introduction of $MnCoO_x$ led to the blocking of micro-pores [2].

SEM was performed to investigate the morphology and microstructure of the as-prepared samples. As shown in Fig. A2, compared with the pure γ-Al_2O_3 catalyst, the presence of nano-laminated structure could be observed on the 5 wt% $MnCoO_x$/γ-Al_2O_3 catalyst, indicating that the manganese oxide and cobalt oxide were successfully impregnated into the γ-Al_2O_3. To further learn the distribution of Mn and Co on the γ-Al_2O_3 surface, EDX dot-mapping was conducted. As depicted in Fig. A3, the high dispersion and uniformity of Mn and Co manifested the well-mixed state of the prepared catalyst. The homogeneous dispersion of active Mn and Co species could be conductive to the toluene decomposition. Moreover, the quantitative analysis demonstrated that the total amount of Mn and Co atom loading was 5.87 wt%, which was approximately in agreement with the ICP results (Table 1).

3.2.2. H_2-TPR analyses

The reducibility of all the as-prepared catalysts was determined using H_2-TPR analysis. As shown in Fig. 5, no reduction peaks of γ-Al_2O_3 were observed in the tested temperature range. As for $MnCoO_x$/γ-Al_2O_3 catalysts, the intensities of the reduction peaks increased with the increasing $MnCoO_x$ loading. The $MnCoO_x$/γ-Al_2O_3 catalysts exhibited similar reduction profiles with two reduction peaks located at temperature ranges of 150–500 °C and 500–800 °C. The large reduction peak at a lower temperature (< 500 °C) could be associated with the stepwise reduction processes of $Mn^{4+} \rightarrow Mn^{3+} \rightarrow Mn^{2+}$ and $Co^{3+} \rightarrow Co^{2+} \rightarrow Co^{\circ}$ [48,49]. This could be attributed to the reduction of multiple phases in the same temperature interval, leading to an overlap of small peaks [32,50]. The broad reduction peak at a high temperature (> 500 °C) could be ascribed to the reduction of Mn-Co mixed oxides [31,51,52]. In the low temperature range (< 200 °C), 5 wt% $MnCoO_x$/γ-Al_2O_3 catalyst was first reduced among the tested catalysts. In addition, the 5 wt% $MnCoO_x$/γ-Al_2O_3 catalyst owned the lowest reduction peak (220 °C), indicating that it is easier to activate oxygen species on its surface [24,45]. This could be conductive to the toluene oxidation, which was in accordance with the results of the catalytic activity.

3.2.3. XPS analyses

The XPS analysis was employed to explore the chemical compositions in the near-surface region of the γ-Al_2O_3 support. The XPS patterns were displayed in Fig. A. 4, Fig. 6, and Table 2. As shown in the XPS spectra for Mn 2p3/2, three main peaks centered at approximately 640.9 eV, 641.9 eV and 643.6 eV were ascribed to the Mn^{2+}, Mn^{3+}, and Mn^{4+} species, respectively [53]. For Co 2p spectra, the Co 2p3/2 peak was divided into two peaks located at approximately 780.3 eV and 782.3 eV, which were assigned to Co^{3+} and Co^{2+}, respectively [53,54]. Quantitatively, the ratios of Mn^{4+}/Mn, Mn^{3+}/Mn and Co^{2+}/Co^{3+} increased initially and then decreased with the increase of $MnCoO_x$ loading, which were calculated on the basis of the peak area. The highest ratios of Mn^{4+}/Mn, Mn^{3+}/Mn and Co^{2+}/Co^{3+} were observed in the 5 wt% $MnCoO_x$/γ-Al_2O_3 catalyst. Previous literature reported that Mn species with higher valence were preferable for the oxidation reactions over Mn-based catalysts [53,55,56]. It also reported that the electron transfer between Mn and Co species was beneficial to the high catalytic oxidation activity [54]. Thus, high ratios of Mn^{4+}/Mn, Mn^{3+}/Mn and Co^{2+}/Co^{3+} were helpful to the catalytic activity for toluene oxidation. The XPS spectra of O1s could be split into two peaks centered at 530.6 eV and 531.8 eV, attributing to the lattice oxygen (O_l) and adsorbed oxygen (O_a), respectively [43,57]. The ratio of O_a/O_l

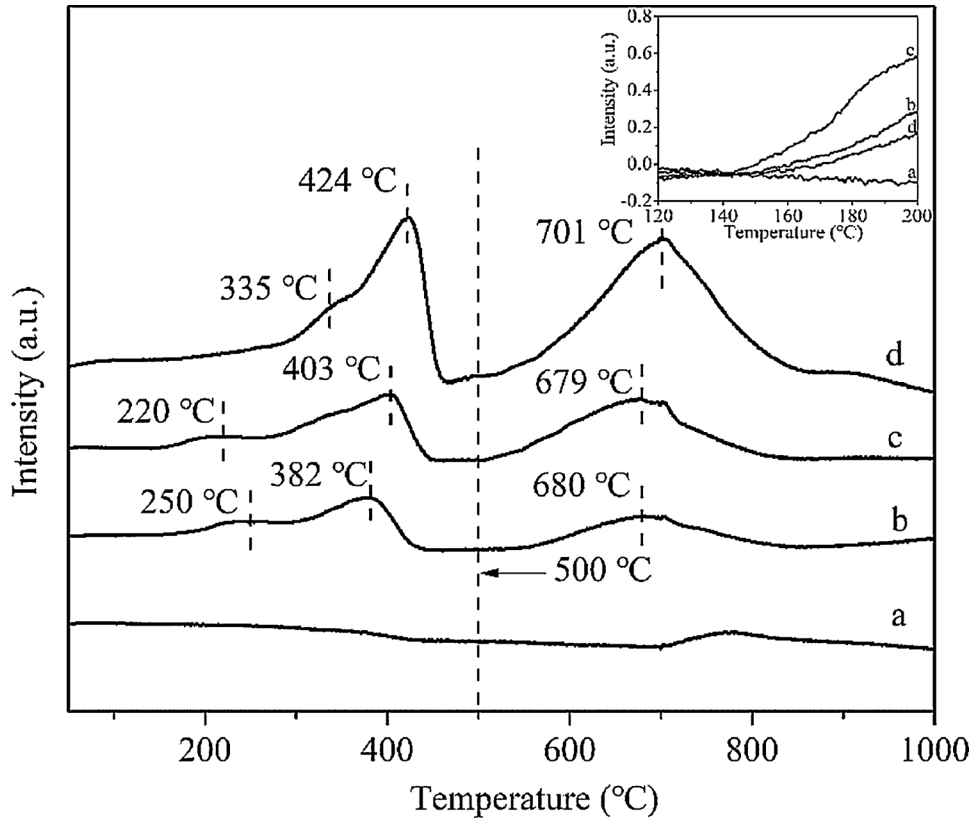

Fig. 5. H_2-TPR profiles of γ-Al_2O_3 and $MnCoO_x$/γ-Al_2O_3 catalysts (a: γ-Al_2O_3, b: 2.5 wt% $MnCoO_x$/γ-Al_2O_3, c: 5 wt% $MnCoO_x$/γ-Al_2O_3, d: 7.5 wt% $MnCoO_x$/γ-Al_2O_3).

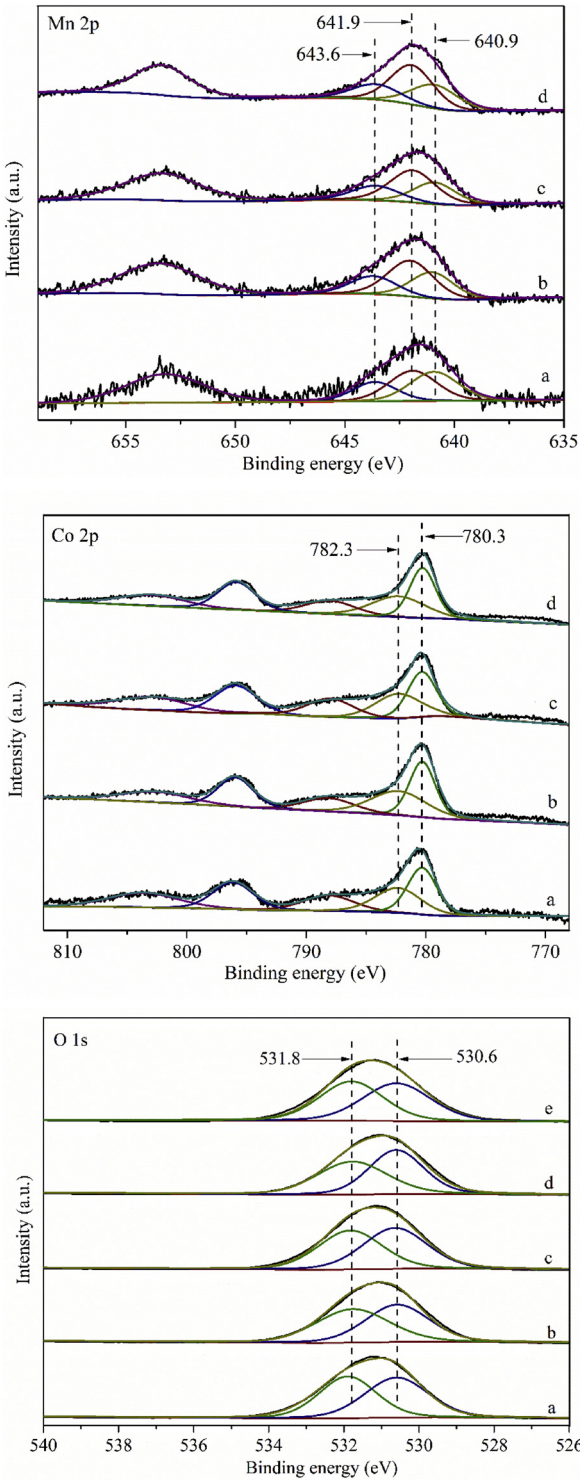

Fig. 6. XPS spectra of γ-Al_2O_3 and $MnCoO_x$/γ-Al_2O_3 catalysts (a: 2.5 wt% $MnCoO_x$/γ-Al_2O_3, b: 5 wt% $MnCoO_x$/γ-Al_2O_3, c: 5 wt% $MnCoO_x$/γ-Al_2O_3 used, d: 7 .5 wt% $MnCoO_x$/γ-Al_2O_3).

increased to the highest when the $MnCoO_x$ loading reached 5% and then decreased. Higher content of O_a could be conductive to generate more active oxygen species, which could markedly enhance the toluene oxidation process [6]. In addition, the amount of O_a decreased after the reaction for 5 wt% $MnCoO_x$/γ-Al_2O_3. This further indicated that oxygen species occupied a vital role in the toluene oxidation process.

As mentioned above, the XRD, Raman and N_2 adsorption-desorption results showed that the $MnCoO_x$/γ-Al_2O_3 catalysts possessed similar

Table 2
XPS analysis of γ-Al_2O_3 and $MnCoO_x$/γ-Al_2O_3 catalysts.

catalyst	Mn^{4+}/ Mn	Mn^{3+}/ Mn	Co^{2+} / Co^{3+}	O_a/O_l
γ-Al_2O_3	–	–	–	0.85
2.5 wt% $MnCoO_x$/γ-Al_2O_3	0.22	0.39	0.83	0.93
5 wt% $MnCoO_x$/γ-Al_2O_3	0.25	0.50	0.93	1.03
5 wt% $MnCoO_x$/γ-Al_2O_3 used	0.23	0.45	0.88	0.95
7.5 wt% $MnCoO_x$/γ-Al_2O_3	0.21	0.47	0.87	0.97

textural properties in terms of approximate crystallinity and surface area. The large surface area of the $MnCoO_x$/γ-Al_2O_3 catalysts could increase the residence time of toluene and intermediates by offering many adsorption sites, thereby resulting in further oxidation of the adsorbed species by active oxygen species on the catalyst surface. The H_2-TPR analyses showed that the content of reducible Mn and Co species increased from 2.5 wt% $MnCoO_x$/γ-Al_2O_3 to 7.5 wt% $MnCoO_x$/γ-Al_2O_3. However, the most favorable catalytic activity was achieved with the 5 wt% $MnCoO_x$/γ-Al_2O_3 catalyst, indicating that the catalytic performance was not exclusively determined by the active center. This phenomenon might be because more active centers were present, making the interaction between the active ingredient and carrier stronger [58]. In addition, the lowest reduction temperature was observed in the 5 wt% $MnCoO_x$/γ-Al_2O_3 catalyst, indicating its easier activation than the other tested catalyst. The XPS profiles showed that the different $MnCoO_x$ loading on the γ-Al_2O_3 could cause changes in their chemical valance. The highest ratios of Mn^{4+}/ Mn, Mn^{3+}/ Mn, Co^{2+}/ Co^{3+}, and O_a/O_l were achieved at 5 wt% $MnCoO_x$/γ-Al_2O_3. The interactions between Mn and Co (Co^{3+} + Mn^{3+} ↔ Co^{2+} + Mn^{4+}) could accelerate the active oxygen mobility [51], which were responsible for the high catalytic oxidation activity. Furthermore, the adsorbed oxygen species could enhance the deep oxidation of toluene and intermediates. Thus, the reducibility and surface active oxygen species of the catalysts occupied a key role in the toluene oxidation process.

The toluene degradation pathway in the post-NTP-catalytic system could be ascribed to the combination of plasma-induced physicochemical reactions and surface oxidation reaction on the $MnCoO_x$/γ-Al_2O_3 catalysts [24,59]. The gas compositions during the reactions in the NTP alone and the post-NTP-catalytic system over the 5 wt% $MnCoO_x$/γ-Al_2O_3 catalyst were analyzed by GC–MS. The discharge power was set as 8 W. As shown in Fig. A. 5, large amounts of organic byproducts were identified in the outlet gas after NTP treated, mainly including 2-butanone, 3,5-di-tertbutylbenzene-1,2-diol, cyclopentanol, 3-methyl-, benzaldehyde, o-xylene, p-xylene, 2-pentanone, hexane, 2-nitro-, nitromethane, undecane, dodecane, nonane, 4-ethyl-5-methyl, 1,3-di-tertbutylbenzene and 2(3 H)-furanone, 5-hexyldihydro-. This result indicated that toluene was incompletely oxidized in the NTP process. Compared to the relative abundance of organic byproducts in the NTP process, it could be found that the types and the total amounts of the organic byproducts greatly decreased with the introduction of the 5 wt% $MnCoO_x$/γ-Al_2O_3 catalyst. Less organic byproducts indicated that toluene and intermediates were further oxidized into CO_2 and CO more completely on the catalyst surface. Combined with previous studies [1,14,19,40], in the NTP process, toluene was attacked by high-energy electrons (1–10 eV) and reactive species (such as $O^{\cdot}$, $OH^{\cdot}$, and $H^{\cdot}$) to form benzyl radical, phenyl radical, methyl and benzaldehyde. The benzyl radical / phenyl radical could react with methyl and / or $OH^{\cdot}$ to form 3,5-di-tertbutylbenzene-1,2-diol, benzaldehyde, o-xylene, p-xylene and 1,3-di-tertbutylbenzene. The benzene ring intermediates were further attacked by high-energy electrons (> 5.5 eV) and active species ($O^{\cdot}$, $OH^{\cdot}$, and $H^{\cdot}$) to form ring-opening products [6]. These ring-opening products could react with methyl to form undecane, dodecane and nonane, 4-ethyl-5-methyl. Meanwhile, they, could react with reactive species (such as $O^{\cdot}$, $OH^{\cdot}$, $H^{\cdot}$, N, and N_2^{*}) to form 2-butanone, cyclopentanol, 3-methyl-, hexane, 2-nitro-, nitromethane and 2(3 H)-furanone. These chain intermediates were further oxidized to

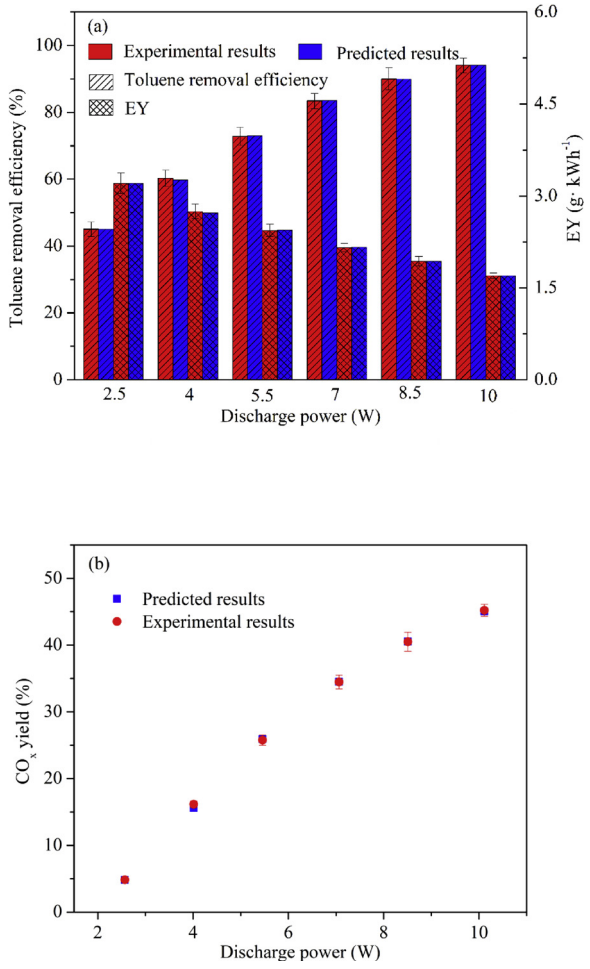

Fig. 7. Effect of discharge power on (a) the toluene removal efficiency and EY, (b) CO_x yield (toluene initial concentration, 54 ppm; gas flow rate, 1.5 L·min^{-1}; RH, 0%).

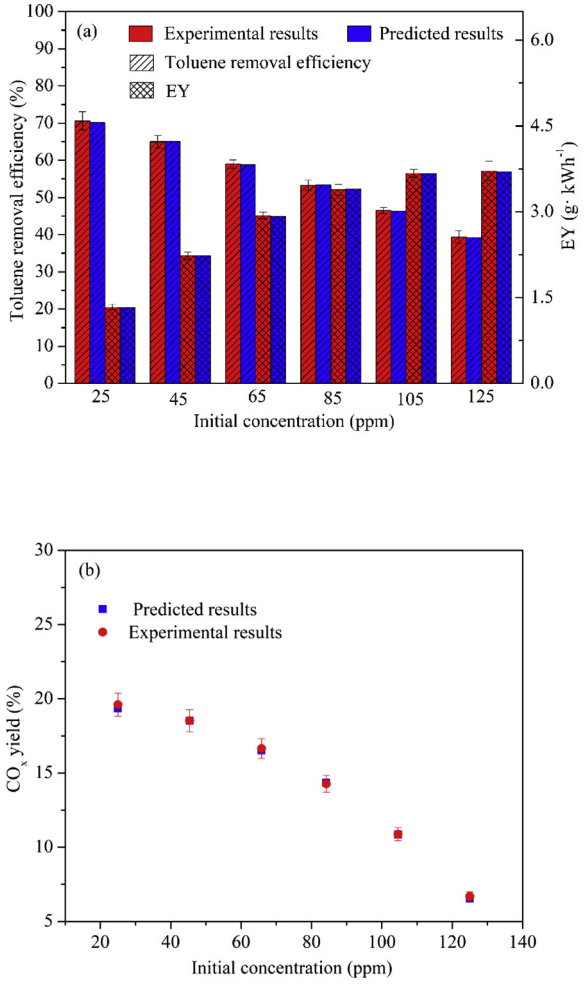

Fig. 8. Effect of initial concentration on (a) the toluene removal efficiency and EY, (b) CO_x yield (discharge power, 4.4 W; gas flow rate, 1.5 L·min^{-1}; RH, 0%).

CO_2, and H_2O ultimately by active species ($O^{\cdot}$, $OH^{\cdot}$). In the catalyst system, toluene and intermediates were adsorbed on the active sites prior to the stepwise oxidation reaction [1]. In general, VOCs oxidation on Mn-based catalysts occurred via the classical Mars–van Krevelen (MVK) mechanism [51,60]. The interactions between Mn and Co oxides could accelerate the surface oxygen mobility and the transition from chemisorbed and lattice oxygen to active oxygen species [40,54]. In addition, O_3 formed in the NTP region could be decomposed by Mn-based catalysts to form active oxygen species [6]. Thus, adsorbed toluene and intermediates were further oxidized by active oxygen species on the catalyst surface to form CO_2 and H_2O.

3.3. Plasma-catalytic removal of toluene

3.3.1. Effect of discharge power

Discharge power is one of the key factors that influence the post-NTP-catalytic process of toluene removal. Fig. 7 showed that the experimental and predicted results agreed well in the post-NTP-catalytic system with 5 wt% $MnCoO_x/\gamma$-Al_2O_3 catalyst as a function of discharge power. The toluene removal efficiency and CO_x yield almost linearly increased with the increase of the discharge power, whereas the EY was negatively correlated with the discharge power. The maximum toluene removal efficiency and CO_x yield of the hybrid system could be achieved at 94.08% and 45.21%, respectively, at the discharge power of 10 W, whereas the maximum EY of 3.21 g·kWh^{-1} was obtained at the discharge power of 2.5 W. This could be attributed to the fact that more high-energy electrons and active species would be generated by higher discharge power, which could accelerate the physicochemical reactions [61,62]. This phenomenon indicated that a cost-effective NTP-catalytic system that could balance the toluene removal and EY should be developed. It was in agreement with the previous studies [1].

3.3.2. Effect of initial concentration of toluene

The effect of the initial toluene concentration on the toluene removal in the post-NTP-catalytic system with 5 wt% $MnCoO_x/\gamma$-Al_2O_3 catalyst was shown in Fig. 8. The simulation results from the ANN model were consistent with the experimental results. The toluene removal efficiency and CO_x yield were negatively correlated with the initial toluene concentration, whereas the EY was positively correlated. The toluene removal efficiency and CO_x yield were of the ranges 70.58%–39.32% and 19.60%–6.68%, respectively, whereas the EY ranged 1.33–3.71 g·kWh^{-1} as the initial toluene concentration ranged from 25 to 125 ppm. The reasons for this phenomenon were as follows: (1) the limited amounts of high-energy electrons and active species generated by the discharge; (2) the limited amounts of active sites formed on the catalyst surface. Thus, the insufficient high-energy electrons, active species and active sites for higher toluene concentration lead to the low reaction performance [24].

3.3.3. Effect of gas flow rate

The gas flow rate occupied an important role in the reaction performance in the post-NTP-catalytic system over 5 wt% $MnCoO_x/\gamma$-Al_2O_3 catalyst. As shown in Fig. 9, the predicted results and experimental results showed a perfect match at different gas flow rates in the hybrid

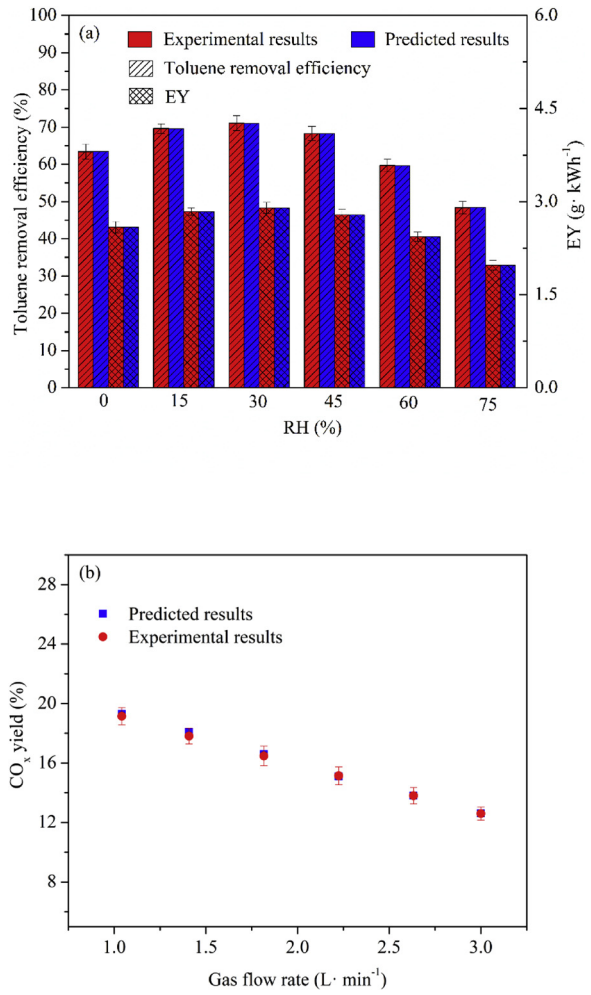

Fig. 9. Effect of gas flow rate on (a) the toluene removal efficiency and EY, (b) CO_x yield (discharge power, 4.4 W; toluene initial concentration, 54 ppm; RH, 0%).

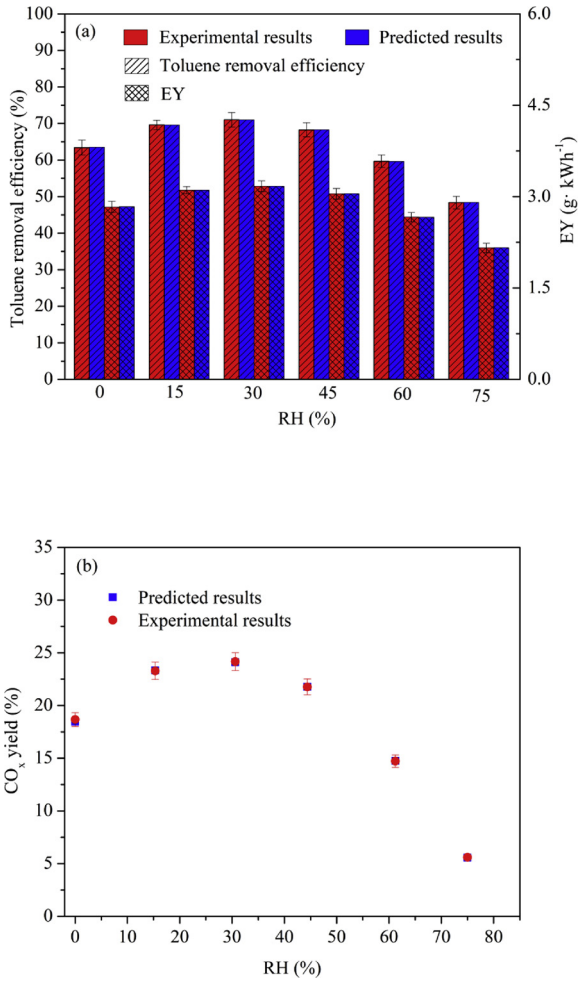

Fig. 10. Effect of RH on (a) the toluene removal efficiency and EY, (b) CO_x yield (discharge power, 4.4 W; toluene initial concentration, 54 ppm; gas flow rate, 1.5 L·min^{-1}).

system. An increase in the gas flow rate led to a lower toluene removal efficiency and CO_x yield, but a higher EY. When the gas flow rate was varied from 1.0 to 3.0 L·min^{-1}, the toluene removal efficiency decreased from 64.38% to 56.56%, the CO_x yield decreased from 19.15% to 12.60%, whereas the EY increased from 1.86 to 4.70 g·kWh^{-1}, respectively. This phenomenon could be interpreted by the following two reasons [6]: (1) The higher gas flow rate improved the toluene concentration per unit time, which could lead to each toluene molecule sharing fewer active species; (2) The gas flow rate increase could reduce the retention time of gas, reducing the collision probabilities between the toluene molecules and reactive species.

3.3.4. Effect of RH

RH exhibited a considerable effect on the performance of the process in the post-NTP-catalytic system with 5 wt% $MnCoO_x/\gamma$-Al_2O_3 catalyst. Fig. 10 showed a perfect match between the experimental and predicted results. The toluene removal efficiency, CO_x yield, and EY increased first and then decreased with the RH increase from 0% to 75%. The highest performance of the system could be achieved at an RH of 30%. This phenomenon could be attributed to the following reasons [62–64]: 1) Water vapor addition could favor the formation of $OH^{\cdot}$ radicals, which could contribute to the toluene oxidation; 2) With an increase in the water vapor, the excess water molecules compete with toluene and intermediates for the adsorption sites of the catalyst, leading to a decrease in toluene removal efficiency; 3) Higher levels of RH could limit the electron density and quench the active species, which could reduce the reaction accessibility between the pollutants and high-energy electrons and active species. In addition, to investigate the stability of 5 wt% $MnCoO_x/\gamma$-Al_2O_3 catalyst in a humid environment (RH, 30%), a long-term durability test was carried out. As shown in Fig. A. 6, at a high space velocity of 90,000 mL·(g·h)$^{-1}$, the toluene removal efficiency and CO_x yield were relatively stable within the reaction time of 100 min, indicating that the 5 wt% $MnCoO_x/\gamma$-Al_2O_3 catalyst had great potential for the elimination of toluene. Also of note was that the catalytic activity decreased gradually with the increasing reaction time. This phenomenon could be attributed to the following reasons [2,21]: (1) with the reaction time increased, more active sites on the catalyst surface were blocked by organic intermediates deposition; (2) more water vapor could quench the active species and occupy the active sites on the catalyst surface.

3.4. Contributions of different experimental parameters

The net weight matrix and Garson equation were used to evaluate the relative importance of each experimental parameter on the reaction performance. As shown in Fig. 11, the discharge power was found to be the most powerful factor influencing the toluene removal efficiency, whereas the influence of the gas flow rate was limited. It indicated that the post-NTP-catalytic system was suitable for the toluene removal with a wide range of gas flow rate. However, for the EY, the gas flow rate occupied a dominant role, followed by initial concentration, discharge power and RH. As for the CO_x yield, the contribution of different

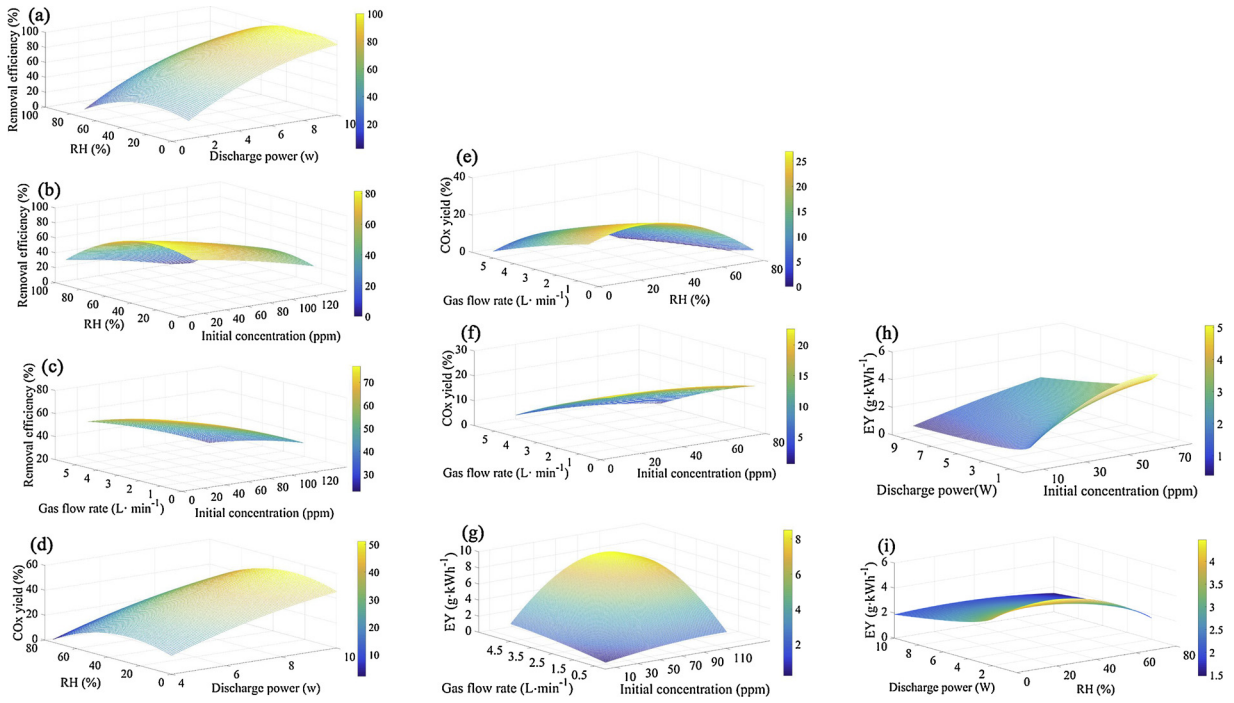

Fig. 11. Effect of different experimental parameters to toluene removal efficiency ((a), (b), (c)) and CO_x yield ((d), (e), (f)) energy yield ((g), (h), (i)).

experimental parameters was as follows: discharge power > RH > gas flow rate > toluene initial concentration.

3.5. Optimal process parameters

The toluene removal efficiency and EY were selected as objectives to optimize the independent variables. The CO_x yield was not selected because its variation trend was similar to that of the toluene removal efficiency. As shown in Fig. 12, any point on the Pareto front corresponded to a set of optimal solutions. The optimal value of the toluene removal efficiency (EY) could be obtained from the given value of EY (the toluene removal efficiency). The front covered a wide range, with 19.70%–100% and 10.13–2.52 g·kWh^{-1} for the toluene removal efficiency and EY, respectively. The optimal solution was distributed uniformly in the range of 50%–100% for the toluene removal efficiency, ensuring the quality of the solution. In addition, the overall variation trend of EY decreased with an increase in the toluene removal efficiency. The EY first decreased gradually first and then decreased rapidly, making 55% toluene removal efficiency a dividing point. This phenomenon indicated that both the toluene removal efficiency and EY were considered when the toluene removal efficiency was approximately 55%.

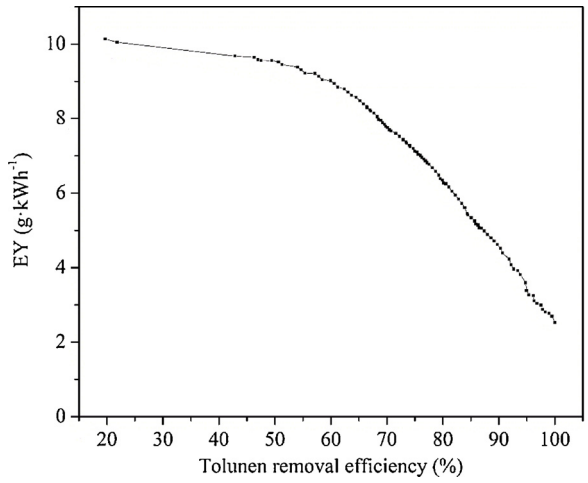

Fig. 12. The first Pareto Front.

4. Conclusions

In this study, toluene removal in the post-NTP-catalytic system over $MnCoO_x/\gamma$-Al_2O_3 catalyst was investigated. The addition of catalyst markedly enhanced the reaction performance compared with the NTP alone system. The 5 wt% $MnCoO_x/\gamma$-Al_2O_3 catalyst demonstrated the best catalytic activity at a discharge power of 10 W. Catalyst characterization such as the reducibility and surface active oxygen species heavily influenced the catalytic activity, which further enhanced the reaction performance.

To explore the effect and importance of different experimental parameters (discharge power, toluene initial concentration, gas flow rate and RH) in the post-NTP-catalytic system over 5 wt% $MnCoO_x/\gamma$-Al_2O_3 catalyst, a hybrid ANN and NSGA-II method was developed. The proper fitting between predicted and experimental results demonstrated that the fast and reliable simulation and prediction of the complex post-NTP-catalytic process could be conducted effectively using the ANN-based model approach. The discharge power was the most important factor that determined the toluene removal and CO_x yield, whereas the gas flow rate accounted for the largest proportion on the EY. A multi-objective optimization model was proposed to determine the optimal experimental parameters, where the toluene removal efficiency and EY were taken as objectives. The problem was solved using the NSGA-II algorithm. The first Pareto front in the results provided an efficient tool to obtain optimal process parameters for customized conditions.

Acknowledgements

This research was financially supported by the National Science Foundation of China (41573138, 41877383), the Fundamental Research Funding for Central Universities in China (xkjc2015002) and China Scholarship Council (No. 201806280087). Yu Huang is also

supported by the “Hundred Talent Program” of the Chinese Academy of Sciences.

Appendix A. Supplementary data

Supplementary material related to this article can be found, in the online version, at doi:https://doi.org/10.1016/j.apcatb.2018.11.025.

References

[1] X.B. Zhu, S.Y. Liu, Y.X. Cai, X. Gao, J.S. Zhou, C.H. Zheng, X. Tu, Post-plasma catalytic removal of methanol over Mn–Ce catalysts in an atmospheric dielectric barrier discharge, Appl. Catal. B: Environ. 183 (2016) 124–132.

[2] X.X. Xu, J.L. Wu, W.C. Xu, M.L. He, M.L. Fu, L.M. Chen, A. Zhu, D.Q. Ye, High-efficiency non-thermal plasma-catalysis of cobalt incorporated mesoporous MCM-41 for toluene removal, Catal. Today 281 (2017) 527–533.

[3] T. Chang, D.X. Ren, Z.X. Shen, Y. Huang, J. Sun, J.J. Cao, J.Y. Zhou, H.X. Liu, H.M. Xu, C.L. Zheng, Indoor air pollution levels in decorated residences and public places over Xi’an, China, Aerosol Air Qual. Res. 17 (2017) 2197–2205.

[4] J. Chen, X. Chen, X. Chen, W.J. Xu, Z. Xu, H.P. Jia, J. Chen, Homogeneous introduction of CeO_y into MnO_x-based catalyst for oxidation of aromatic VOCs, Appl. Catal. B: Environ. 224 (2018) 825–835.

[5] N. Xu, W.N. Fu, C. He, L.F. Cao, X.H. Liu, J.L. Zhao, H. Pan, Benzene removal using non-thermal plasma with CuO/AC catalyst: reaction condition optimization and decomposition mechanism, Plasma Chem. Plasma P 34 (2014) 1387–1402.

[6] B.W. Wang, C.C.Chi.M. Xu, C. Wang, D.J. Meng, Plasma-catalytic removal of toluene over CeO_2-MnO_x catalysts in an atmosphere dielectric barrier discharge, Chem. Eng. J. 322 (2017) 672–692.

[7] Y. Huang, Y.L. Liang, Y.F. Rao, D.D. Zhu, J.J. Cao, Z.X. Shen, W.K. Ho, S.C. Lee, Environment-friendly carbon quantum Dots/$ZnFe_2O_4$ photocatalysts: characterization, biocompatibility, and mechanisms for NO removal, Environ. Sci. Technol. 51 (2017) 2924–2933.

[8] Y. Huang, Y.X. Gao, Q. Zhang, Y.F. Zhang, J.J. Cao, W.K. Ho, S.C. Lee, Biocompatible FeOOH-Carbon quantum dots nanocomposites for gaseous NO_x removal under visible light: improved charge separation and High selectivity, J. Hazard. Mater. 354 (2018) 54–62.

[9] Y.M. Liu, H. Ren, H. Lv, J. Guang, Y.F. Cao, Synthesis of magnetic $Bi_2O_2CO_3$/$ZnFe_2O_4$ composite with improved photocatalytic activity and easy recyclability, Appl. Surf. Sci. 433 (2018) 610–616.

[10] X.X. Xu, P.T. Wang, W.C. Xu, J.L. Wu, L.M. Chen, M.L. Fu, D.Q. Ye, Plasma-catalysis of metal loaded SBA-15 for toluene removal: comparison of continuously introduced and adsorption-discharge plasma system, Chem. Eng. J. 283 (2016) 276–284.

[11] C.A.B.K.B. Schnelle Jr, Air Pollution Control Technology Handbook, Crc Press, 2001.

[12] N. Jiang, N. Lu, K.F. Shang, J. Li, Y. Wu, Innovative approach for benzene degradation using hybrid surface/packed-bed discharge plasmas, Environ. Sci. Technol. 47 (2013) 9898–9903.

[13] X.B. Zhu, S. Zhang, Y. Yang, C.H. Zheng, J.S. Zhou, X. Gao, X. Tu, Enhanced performance for plasma-catalytic oxidation of ethyl acetate over $La_{1-x}Ce_xCoO_{3+\delta}$ catalysts, Appl. Catal. B: Environ. 213 (2017) 97–105.

[14] H.B. Huang, D.Q. Ye, D.Y.C. Leung, F.D. Feng, X.J. Guan, Byproducts and pathways of toluene destruction via plasma-catalysis, J. Mol. Catal. A Chem. 336 (2011) 87–93.

[15] A. Maciuca, C. Batiot-Dupeyrat, J.-M. Tatibouët, Synergetic effect by coupling photocatalysis with plasma for low VOCs concentration removal from air, Appl. Catal. B: Environ. 125 (2012) 432–438.

[16] W.J. Liang, A.H. Wang, L. Ma, J. Li, Combination of spontaneous polarization plasma and photocatalyst for toluene oxidation, J. Electrostat. 75 (2015) 27–34.

[17] N. Jiang, J. Hu, J. Li, K.F. Shang, N. Lu, Y. Wu, Plasma-catalytic degradation of benzene over Ag–Ce bimetallic oxide catalysts using hybrid surface/packed-bed discharge plasmas, Appl. Catal. B: Environ. 184 (2016) 355–363.

[18] J.V. Durme, J. Dewulf, C. Leys, H.V. Langenhove, Combining non-thermal plasma with heterogeneous catalysis in waste gas treatment: a review, Appl. Catal. B: Environ. 78 (2008) 324–333.

[19] A.M. Vandenbroucke, M. Mora, C. Jiménez-Sanchidrián, F.J. Romero-Salguero, N.D. Geyter, C. Leys, R. Morent, TCE abatement with a plasma-catalytic combined system using MnO_2 as catalyst, Appl. Catal. B: Environ. 156 (2014) 94–100.

[20] M.N. Lyulyukin, A.S. Besov, A.V. Vorontsov, Acetone and ethanol vapor oxidation via negative atmospheric corona discharge over titania-based catalysts, Appl. Catal. B: Environ. 183 (2016) 18–27.

[21] J.L. Wu, Q.B. Xia, H.H. Wang, Z. Li, Catalytic performance of plasma catalysis system with nickel oxide catalysts on different supports for toluene removal: effect of water vapor, Appl. Catal. B: Environ. 156-157 (2014) 265–272.

[22] M. Schiavon, V. Torretta, A. Casazza, M. Ragazzi, Non-thermal plasma as an innovative option for the abatement of volatile organic compounds: a review, Water Air Soil Pollut. Focus. 228 (2017) 388–407.

[23] Y.Z. Li, Z.Y. Fan, J.W. Shi, Z.Y. Liu, J.W. Zhou, W.F. Shangguan, Modified manganese oxide octahedral molecular sieves M′-OMS-2 (M′ = Co,Ce,Cu) as catalysts in post plasma-catalysis for acetaldehyde degradation, Catal. Today 256 (2015) 178–185.

[24] X.B. Zhu, X. Tu, D.H. Mei, C.H. Zheng, J.S. Zhou, X. Gao, Z.Y. Luo, M.J. Ni, K.F. Cen, Investigation of hybrid plasma-catalytic removal of acetone over CuO/gamma-Al_2O_3 catalysts using response surface method, Chemosphere 155 (2016) 9–17.

[25] Z. Ye, J.-M. Giraudon, N. Nuns, P. Simon, N. De Geyter, R. Morent, J.-F. Lamonier, Influence of the preparation method on the activity of copper-manganese oxides for toluene total oxidation, Appl. Catal. B: Environ. 223 (2017) 154–166.

[26] H. Ranji-Burachaloo, S. Masoomi-Godarzi, A.A. Khodadadi, Y. Mortazavi, Synergetic effects of plasma and metal oxide catalysts on diesel soot oxidation, Appl. Catal. B: Environ. 182 (2016) 74–84.

[27] R. Craciun, B. Nentwick, K. Hadjiivanov, H. Knözinger, Structure and redox properties of MnO_x/Yttrium-stabilized zirconia (YSZ) catalyst and its used in CO and CH_4 oxidation, Appl. Catal. A Gen. 243 (2003) 67–79.

[28] X.Y. Du, C.T. Li, L.K. Zhao, J. Zhang, L. Gao, J.J. Sheng, Y.Y. Yi, J.Q. Chen, G.M. Zeng, Promotional removal of HCHO from simulated flue gas over Mn-Fe oxides modified activated coke, Appl. Catal. B: Environ. 232 (2018) 37–48.

[29] S.H. Xie, Y.X. Liu, J.G. Deng, X.T. Zhao, J. Yang, K.F. Zhang, Z. Han, H. Arandiyan, H.X. Dai, Effect of transition metal doping on the catalytic performance of Au–Pd/3DOM Mn_2O_3 for the oxidation of methane and o-xylene, Appl. Catal. B: Environ. 206 (2017) 221–232.

[30] H.W. Li, T.T. Huang, Y.F. Lu, L. Cui, Z.Y. Wang, C.F. Zhang, S.C. Lee, Y. Huang, J.J. Cao, W.K. Ho, Unraveling the mechanisms of room-temperature catalytic degradation of indoor formaldehyde and its biocompatibility on colloidal TiO_2-supported MnO_x–CeO_2, Environ. Sci. Nano 5 (2018) 1130–1139.

[31] S. Todorova, H. Kolev, J.P. Holgado, G. Kadinov, R. Ch. Bonev, A. Peren˜ı´guez, Caballero complete n-hexane oxidation over supported Mn–Co catalysts, Appl. Catal. B: Environ. 94 (2010) 46–54.

[32] Z.P. Qu, K. Gao, Q. Fu, Y. Qin, Low-temperature catalytic oxidation of toluene over nanocrystal-like Mn–Co oxides prepared by two-step hydrothermal method, Catal. Commun. 52 (2014) 31–35.

[33] Z.Y. Tian, P.H. Tchoua Ngamou, V. Vannier, K. Kohse-Höinghaus, N. Bahlawane, Catalytic oxidation of VOCs over mixed Co–Mn oxides, Appl. Catal. B: Environ. 117-118 (2012) 125–134.

[34] C. He, J.J. Li, P. Li, J. Cheng, Z.P. Hao, Z.P. Xu, Comprehensive investigation of Pd/ZSM-5/MCM-48 composite catalysts with enhanced activity and stability for benzene oxidation, Appl. Catal. B: Environ. 96 (2010) 466–475.

[35] C.H. Zhang, C. Wang, S. Gil, A. Boreave, L. Retailleau, Y.L. Guo, J.L. Valverde, A. Giroir-Fendler, Catalytic oxidation of 1,2-dichloropropane over supported $LaMnO_x$ oxides catalysts, Appl. Catal. B: Environ. 201 (2017) 552–560.

[36] P. Lakshmanan, L. Delannoy, V. Richard, C. Méthivier, C. Potvin, C. Louis, Total oxidation of propene over Au/xCeO_2-Al_2O_3 catalysts: influence of the CeO_2 loading and the activation treatment, Appl. Catal. B: Environ. 96 (2010) 117–125.

[37] Z.P. Ye, S.K.P. Veerapandian, I. Onyshchenko, A. Nikiforov, N.D. Geyter, J.-M. Giraudon, J.-F. Lamonier, R. Morent, An in-depth investigation of toluene decomposition with a glass beads-packed bed dielectric barrier discharge reactor, Ind. Eng. Chem. Res. 56 (2017) 10215–10226.

[38] S.Y. Liu, D.H. Mei, Z. Shen, X. Tu, Nonoxidative conversion of methane in a dielectric barrier discharge reactor: prediction of reaction performance based on neural network model, J. Phys. Chem. C 118 (2014) 10686–10693.

[39] A. Istadi, N.A.S. Amin, Hybrid artificial neural network – Genetic algorithm technique for modeling and optimization of plasma reactor, Ind. Eng. Chem. Res. 45 (2006) 6655–6664.

[40] T. Chang, Z.X. Shen, Y. Huang, J.Q. Lu, D.X. Ren, J. Sun, J.J. Cao, H.X. Liu, Post-plasma-catalytic removal of toluene using MnO_2–Co_3O_4 catalysts and their synergistic mechanism, Chem. Eng. J. 348 (2018) 15–25.

[41] J.L. Wu, J. Li, J. Li, Y.Q. Jin, Abatement of toluene from gas streams via ferroelectric packed bed dielectric barrier discharge plasma, J. Hazard. Mater. 170 (2009) 633–638.

[42] M.T.N. Dinh, J.M. Giraudon, A.M. Vandenbroucke, R. Morent, N.D. Geyter, J.F. Lamonier, Post plasma-catalysis for total oxidation of trichloroethylene over Ce–Mn based oxides synthesized by a modified “redox-precipitation route”, Appl. Catal. B: Environ. 172-173 (2015) 65–72.

[43] C. Shi, Y. Wang, A. Zhu, B.B. Chen, C. Au, $Mn_xCo_{3-x}O_4$ solid solution as high-efficient catalysts for low-temperature oxidation of formaldehyde, Catal. Commun. 28 (2012) 18–22.

[44] W.X. Tang, X.F. Wu, S.D. Li, W.H. Li, Y.F. Chen, Porous Mn–Co mixed oxide nanorod as a novel catalyst with enhanced catalytic activity for removal of VOCs, Catal. Commun. 56 (2014) 134–138.

[45] G.L. Zhou, X.L. He, S. Liu, H.M. Xie, M. Fu, Phenyl VOCs catalytic combustion on supported CoMn/AC oxide catalyst, J. Ind. Eng. Chem. 21 (2015) 932–941.

[46] T. Wang, S. Chen, H.Q. Wang, Z. Liu, Z.B. Wu, In-plasma catalytic degradation of toluene over different MnO_2 polymorphs and study of reaction mechanism, Chin.J. Catal. 38 (2017) 793–803.

[47] Z.Y. Tian, P.H.T. Ngamou, V. Vannier, K. Kohse-Höinghaus, N. Bahlawane, Catalytic oxidation of VOCs over mixed Co–Mn oxides, Appl. Catal. B: Environ. 117-118 (2012) 125–134.

[48] C. Shi, Y. Wang, A. Zhu, B.B. Chen, C.T. Au, $Mn_xCo_{3-x}O_4$ solid solution as high efficient catalysts for low temperature oxidation of formaldehyde, Catal. Commun. 28 (2012) 18–22.

[49] M.H. Castaño, R. Molina, S. Moreno, Cooperative effect of the Co–Mn mixed oxides for the catalytic oxidation of VOCs: influence of the synthesis method, Appl. Catal. A Gen. 492 (2015) 48–59.

[50] H.W. Liang, H.Q. Sun, A. Patel, P. Shukla, Z.H. Zhu, S.B. Wang, Excellent performance of mesoporous Co_3O_4-MnO_2 nanoparticles in heterogeneous activation of peroxymonosulfate for phenol degradation in aqueous solutions, Appl. Catal. B: Environ. 127 (2012) 330–335.

[51] S. Todorova, A. Naydenov, H. Kolev, J.P. Holgado, G. Ivanov, G. Kadinov, A. Caballero, Mechanism of complete n-hexane oxidation on silica supported cobalt and manganese catalysts, Appl. Catal. A Gen. 413-414 (2012) 43–51.

[52] M.Y. Qiu, S.H. Zhan, H.B. Yu, D.D. Zhu, Low-temperature selective catalytic reduction of NO with NH_3 over ordered mesoporous $Mn_xCo_{3-x}O_4$ catalyst, Catal. Commun. 62 (2015) 107–111.
[53] M.Z. Wu, W.C. Zhan, Y.L. Guo, Y. Guo, Y.S. Wang, L. Wang, G.Z. Lu, An effective Mn-Co mixed oxide catalyst for the solvent-free selective oxidation of cyclohexane with molecular oxygen, Appl. Catal. A Gen. 523 (2016) 97–106.
[54] X.L. Tang, F.Y. Gao, Y. Xiang, H.H. Yi, S.Z. Zhao, Low temperature catalytic oxidation of nitric oxide over the Mn–CoO_x catalyst modified by nonthermal plasma, Catal. Commun. 64 (2015) 12–17.
[55] Q. Ye, J.S. Zhao, F.F. Huo, D. Wang, S.Y. Cheng, T.F. Kang, H.X. Dai, Nanosized Au supported on three-dimensionally ordered mesoporous β-MnO_2: highly active catalysts for the low-temperature oxidation of carbon monoxide, benzene, and toluene, Microporous Mesoporous Mater. 172 (2013) 20–29.
[56] J. Zhou, L.F. Qin, W. Xiao, C. Zeng, N. Li, T. Lv, H. Zhu, Oriented growth of layered-MnO_2 nanosheets over α-MnO_2 nanotubes for enhanced room-temperature HCHO oxidation, Appl. Catal. B: Environ. 207 (2017) 233–243.
[57] G.X. Zhu, J.G. Zhu, W.J. Jiang, Z.J. Zhang, J. Wang, Y.F. Zhu, Q.F. Zhang, Surface oxygen vacancy induced α-MnO_2 nanofiber for highly efficient ozone elimination, Appl. Catal. B: Environ. 209 (2017) 729–737.
[58] M.J. Lu, R. Huang, J.L. Wu, M.L. Fu, L.M. Chen, D.Q. Ye, On the performance and mechanisms of toluene removal by FeO_x/SBA-15-assisted non-thermal plasma at atmospheric pressure and room temperature, Catal. Today 242 (2015) 274–286.
[59] M.T.N. Dinh, J.M. Giraudon, J.F. Lamonier, A. Vandenbroucke, N.D. Geyter, C. Leys, R. Morent, Plasma-catalysis of low TCE concentration in air using $LaMnO_{3+\delta}$ as catalyst, Appl. Catal. B: Environ. 147 (2014) 904–911.
[60] J.P. Durand, S.D. Senanayake, S.L. Suib, D.R. Mullins, Reaction of formic acid over amorphous manganese oxide catalytic systems: an in situ study, J. Phys. Chem. C 114 (2010) 20000–20006.
[61] Y.X. Zeng, L. Wang, C.F. Wu, J.Q. Wang, B.X. Shen, X. Tu, Low temperature reforming of biogas over K-, Mg- and Ce-promoted Ni/Al_2O_3 catalysts for the production of hydrogen rich syngas: understanding the plasma-catalytic synergy, Appl. Catal. B: Environ. 224 (2018) 469–478.
[62] S.Y. Liu, D.H. Mei, L. Wang, X. Tu, Steam reforming of toluene as biomass tar model compound in a gliding arc discharge reactor, Chem. Eng. J. 307 (2017) 793–802.
[63] G. Costa, A.A. Assadi, S.G.-A. Ghaida, A. Bouzaza, D. Wolbert, Study of butyraldehyde degradation and by-products formation by using a surface plasma discharge in pilot scale: process modeling and simulation of relative humidity effect, Chem. Eng. J. 307 (2017) 785–792.
[64] H.B. Huang, D.Q. Ye, D.Y.C. Leung, IEEE Trans. Plasma Sci. 39 (2011) 576–580.